Annales Geophysicae (2004) 22: 1–14
SRef-ID: 1432-0576/ag/2004-22-1

Annales Geophysicae

The OI 630.0 and 557.7 nm dayglow measured by WINDII and modeled by TRANSCAR

F. Culot[1], **C. Lathuillère**[1], **J. Lilensten**[1], **and O. Witasse**[2]

[1]Laboratoire de Planétologie de Grenoble, Bâtiment D de physique, B.P. 53, 38041 Grenoble cedex 9, France
[2]ESA ESTEC, PO Box 299, 2200 AG Noordwijk, The Netherlands

Received: 10 October 2003 – Revised: 16 January 2004 – Accepted: 2 February 2004 – Published:

Abstract. A 1-D fluid/kinetic code is used to model WIND Imaging Interferometer measurements of the atomic oxygen (^{3}P-^{1}D) red and (^{1}D-^{1}S) green thermospheric dayglows at 630.0 nm and 557.7 nm. This modelling is performed for different latitude and solar zenith angle conditions, in order to reproduce the measurements all along the satellite orbit. Results are successfully compared to the interferometer's observations, reproducing the measured volume emission rates, together with the maximum emission altitude. A good agreement is found regardless of the position considered along the satellite orbit, meaning that the solar flux and the solar zenith angle influences were successfully taken into account. Together with this model study, a four-year red and green oxygen lines set of WINDII data is analysed with regards to those geophysical parameters. Correlations between volume emission rates and solar flux are evaluated and it is found that the $MgII$ index is better suited to this kind of study than the $f_{10.7}$ decimetric index.

Key words. Atmospheric composition and structure (airglow and aurora; thermosphere – composition and chemistry) – Ionosphere (modeling and forecasting)

1 Introduction

Studying the atmosphere's airglow emissions is a broad research topic, which provides valuable information about the chemical and dynamical processes controlling the state of the upper mesosphere and lower thermosphere. Even if this aeronomic research field is quite new (the word "airglow" was first used by Chamberlain (1961)), a number of studies have been done to examine the various upper atmosphere emissions. Among those emissions, the O(^{1}D) 630.0 nm red and O(^{1}S) 557.7 nm green atomic oxygen lines are the most intense and, therefore, have been the subject of numerous studies, using two complementary approaches: observations involving ground-based rocket and satellite techniques, and modeling. We focus on the thermospheric dayglow. Most of the available data were obtained either from the visible airglow instrument (Hays et al., 1973), or from the WIND Imaging Interferometer (WINDII) (Shepherd et al., 1993), that we will use here. Ground-based daytime observations are more recent because of detection problems due to the presence of a high solar background against a faint dayglow emission. The first studies were made possible with the development of dayglow photometers (DGP) (Narayanan et al., 1989) and multi-wavelength daytime photometers (MWDPM) (Sridharan et al., 1998). In a very recent paper, Taori et al. (2003) discussed simultaneous ground-based observations of red and green dayglow and outlined the significant importance of the thermospheric contribution to the 557.7 nm emission, as already shown by rocket and satellite measurements.

The complementary approach to measurements is modeling: the different line excitation processes begin to be well understood, as shown by the confrontation of the modelling to the observations. Several papers review such works, among them (Solomon and Abreu, 1989) for the red line and (Singh et al., 1996) for the green line. Most of the recent studies try to model WINDII observations whose database covers several years, including all geophysical conditions. However, most of these studies focus on a limited set of data. Among the most recent ones, Tyagi and Singh (1998), using the Solomon's glow model, have shown a reasonable agreement between modelled data and a morphological picture of WINDII observations of the greenline dayglow obtained between December 1992 and April 1993. Witasse et al. (1999) modeled both the red and green lines emissions for EISCAT-WINDII correlated observations and highlighted the need for renewed measurements of the EUV solar spectrum, that is one of the main input to any glow model.

In addition to this input, some of the reaction rate coefficients are still under debate. For example, a new temperature dependant rate coefficient for the reaction $N_2(A^3\Sigma_u^+)+O$, is proposed by Hill et al. (2000). The Upadhayaya and Singh (2002) and the Singh and Tyagi (2002) papers outline the resulting ambiguity. They discuss both the EUV spectrum

Correspondence to: F. Culot
(frederic.culot@obs.ujf-grenoble.fr)

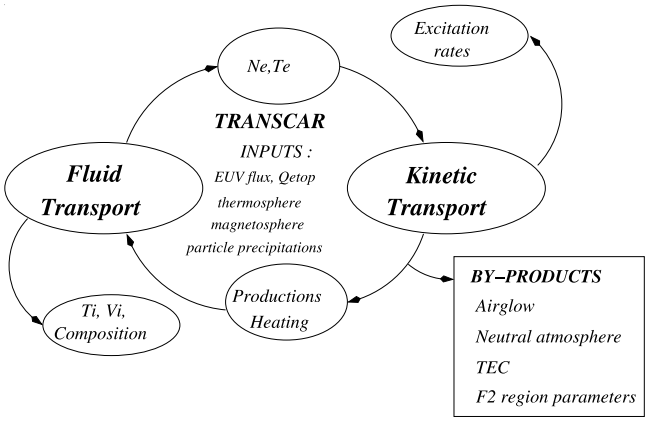

Fig. 1. Synopsis of the TRANSCAR model.

model and the Hill et al. (2000) new temperature dependant coefficient for best representing WINDII dayglow emissions.

Our work comes naturally in this modelling perspective but aims to give a more global picture of the thermospheric WINDII measurements over its 5 first years of observations, and moreover to discuss the current ability to model the main features that are observed. For this purpose, we focus on the altitude and intensity (Volume Emission Rate - VER) of the 630.0 nm dayglow and of the thermospheric layer of the 555.7 nm dayglow, for which a statistical analysis over 5 years is done. We model the WINDII observations along the satellite orbit meaning that we take into account the coupled influence of local time (or Solar Zenith Angle – SZA) and latitude. This is done for high and low solar activity and for both emissions.

The TRANSCAR model and its glow added software (Witasse et al., 1999) that we use here, is presented in the first section. It has shown its ability to correctly describe high latitude measurements but needs to be tested against other geophysical conditions and latitudes. The calculation of the peak and intensity of the thermospheric emissions from WINDII instrument is described in the second section. Then, the results obtained from the modelling of the oxygen emissions along the WINDII orbit are discussed. Finally, the statistical behaviour of the thermospheric red and green oxygen line emissions is presented, as a function of the two main geophysical parameters that characterize them: the solar zenith angle and the solar activity. This statistical study is limited to periods of quiet magnetic activity.

2 TRANSCAR model

A complete description of TRANSCAR can be found in Lilensten and Blelly (2002), including the most recent enhancements. Only the global structure of the code will be recalled here. However, the model was run only for high latitudes until now, and thus a discussion about why it's use can be extended to mid- and low-latitudes is included after the model presentation.

2.1 Model description

To give a brief overview of the code, one can say that TRANSCAR is based on the coupling of two models:

- A one-dimensional time-dependant fluid model of the ionosphere which solves the temporal evolution of the lower moments: concentration, velocity, temperature and heat flow of the isotropic distribution function of six ions (O_2^+, N_2^+, NO^+, O^+, H^+ and N^+) and electrons
- A kinetic model which solves the energetic electron transport equation and provides electron heating and ion production rates.

The dynamically coupling of both parts of TRANSCAR is illustrated by the synopsis in Fig. 1.

Concerning the photochemical model used to simulate the red and green oxygen lines emissions, all of the production and loss processes with the corresponding rates for the O(^{1}D) and O(^{1}S) states are given in Witasse et al. (1999). The main reactions used in the model are summarized in Table 1. Figure 2 is a scheme that shows the relative contributions of these major processes. This scheme represents the oxygen red and green lines at mid-latitudes (around 45°), at around 12:00 local time, and for weak solar activity ($f_{10.7}\sim$120) and weak magnetic activity ($A_p\leq$10). The most important production processes at the maximum of the layers are the photoelectron impacts and the collisional deactivation of N_2 for the 557.7 nm thermospheric emission, and the dissociative recombination, together with the photoelectron impacts for the 630.0 nm emission.

Using the TRANSCAR model, Witasse et al. (1999) computed the oxygen thermospheric dayglow at high latitude (Tromsø, 69.6° N). They first compared the modelled ionosphere to European Incoherent Scatter (EISCAT) radar measurements. This allowed one to calibrate the neutral atmosphere. Then, they compared the airglow results with WINDII data. In the present work, no calibration of the neutral atmosphere is performed. The vertical profiles of the major neutral components are taken directly from the empirical model MSIS-90 (Hedin, 1991), and the EUVAC model (Richards et al., 1994) is used to provide the solar EUV flux. Electron density and temperature, ion densities and temperatures, as well as O(^{1}D) and O(^{1}S) emission rates, are calculated consistently within the model throughout the whole thermosphere altitude range without the use of any other empirical model than the two cited above. Lathuillere et al. (2002) have shown that the MSIS-90 model was fully consistent with thermospheric temperatures deduced from O(^{1}D) WINDII measurements for quiet magnetic activity periods and have pointed out that the MSIS-90 model underestimates these temperatures for large magnetic activity. Therefore, we have limited the present study to days with low magnetic activity. A discussion about the choice of the solar EUV model

Table 1. Main production processes used in TRANSCAR for the red and green atomic oxygen lines.

630 nm red line	557.7 nm green line
Electron impact $O + e_{ph} \rightarrow O(^1D) + e_{ph}$	Electron impact $O + e_{ph} \rightarrow O(^1S) + e_{ph}$
Photodissociation of O_2 molecules $O_2 + h\nu \rightarrow O + O(^1D)$	Photodissociation of O_2 molecules $O_2 + h\nu \rightarrow O + O(^1S)$
Dissociative recombination $O_2^+ + e_{th} \rightarrow O + O(^1D)$	Collisional deactivation of N_2 $N_2(A^3\Sigma_u^+) + O \rightarrow N_2 + O(^1S)$

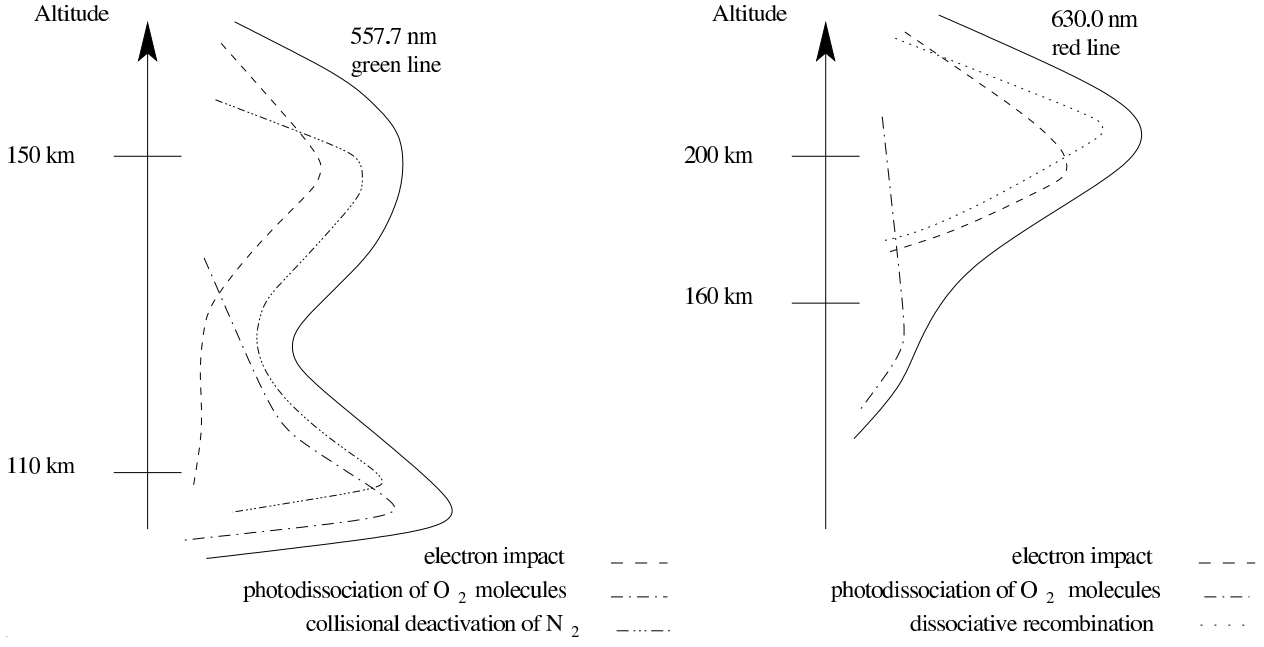

Fig. 2. Relative contributions of processes involved in the green (left-hand side) and red (right-hand side) atomic oxygen day time emissions (after Witasse et al., 1999). This scheme stands for solar conditions with $f_{10.7}$~120, low magnetic activity (A_p<10) and at 12:00 LT.

in TRANSCAR can be found in Lilensten and Blelly (2002) and Witasse et al. (1999).

In this study, we model the oxygen emissions along a whole satellite orbit, that corresponds to the zonal mean of a given day as described below. Each point was obtained after the TRANSCAR simulation was run for 10 h (in local time) in order to reduce dependence on initial conditions and to be sure to be in a steady-state situation. The fluid equations are solved every second to provide the electron temperature and concentration, and the kinetic code is called every five minutes, in order to regenerate the heating rates and ion productions.

2.2 Use of TRANSCAR at mid- and low-latitudes

The geometry of the physics is different in the nightside and in the dayside. In the nightside, the electrons are coming along the geomagnetic lines and any secondary electron due to ionisation through impact is driven along the geomagnetic line. The secondary electron angular phase function is strongly forward peaked, while the primary electron keeps its initial direction (Opal et al., 1971). The movement may be upward or downward. The pitch angle under which the incident electron collide with a neutral target is reflecting the fact that the electrons rotate around the local line of force, while the centre of mass follows the line of force. Therefore, in the nightside, the natural geometry is to describe the movement along the **B** field. Any projection along the altitude axis is not possible when the two are perpendicular. At low latitude, the fact that the line of force is almost perpendicular to the pressure gradient introduces some error that has not been carefully quantified yet.

The problem has to be reconsidered in the dayside of the Earth. The reason is that the primary source of electrons is the solar XUV-EUV flux. The natural geometry is then the line of sight between the observation altitude and the Sun. The projection along the vertical axis is taken into account through a Chapman function. When a photoionisation occurs, the primary photoelectron is created in any direc-

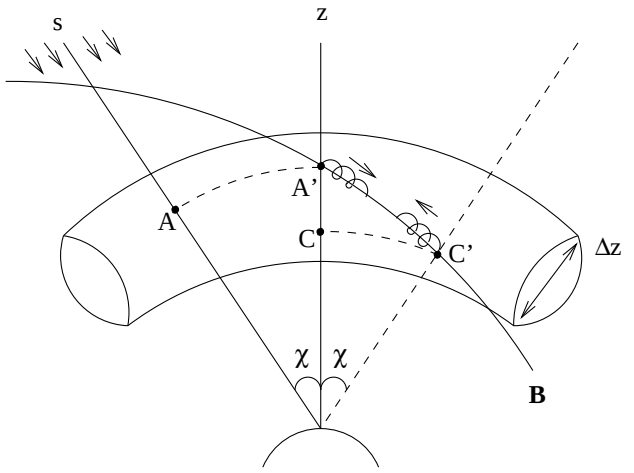

Fig. 3. Problem Geometry. The axis s is the solar-terrestrial axis. At an observation point at the surface of the Earth, the solar zenith angle is χ. The vertical axis at this point is z. The local magnetic field line is represented by the symbol **B**, and we consider an atmospheric slab of thickness dz.

tion: the angular phase function is simply isotropic. Then, when this primary electron creates a secondary production through impact, the secondary electron is forward peaked, but since the primary electron comes from any direction, the result is that on average, the secondary electrons have an isotropic distribution. This fact has a tremendous impact on the physics. We may consider 2 steps illustrated in Figs. 3 and 4.

In Fig. 3, we consider an atmosphere slab. It is characterized by a single density value (actually, one per species), a single temperature, and a single magnetic angle value. The line of sight is s, the vertical axis is z. A photoelectron created in A is projected on the z axis by a Chapman function (point A$'$). There, the motion of its centre of force is along the local magnetic line. The isotropy means here that its pitch angle is isotropically distributed. Let us consider that it goes down with an angle μ (with a projection). In the same slab, an electron created in C would be projected in C$'$ with an isotropically distributed pitch angle. Its probability to go upward along the local magnetic line with the pitch angle μ is exactly the same ($1/4\pi$) as the first electron to escape A$'$ downward with a pitch angle μ. The conclusion of this geometry is that in A$'$, there are as many photoelectrons going in any direction.

To envision the following, we consider Fig. 4. The question is now "on which projection is there a variation in the stationary electron flux?". This means that we are now not dealing with the photoproduction but with the electron transport, i.e. with the Boltzmann equation. In Fig. 4a, we consider an horizontal projection. On the basis of what precedes, the horizontal projection of a secondary electron created in A$'$ by a collision between a photoelectron (isotropically created) and a neutral is exactly compensated by a secondary electron coming from the point D$'$. This is a consequence of the isotropy of the photoelectrons (which are now the ionization source). This is also a consequence of the fact that we suppose that the atmosphere is horizontally stratified (or, as in Fig. 3, stratified parallel to the surface of the Earth). Therefore, there is no information in the horizontal axis on the variation of the stationary electron flux.

In Fig. 4b, we look at the vertical projection. An electron which escapes the point A$'$ in a given altitude slab to the lower (respectively larger) altitudes meets a denser (or weaker) atmosphere. Its absorption by inelastic collision increases as the collision depth increases. Therefore, it cannot be compensated by an electron coming from a point E$'$ in the closest lower slab. In short, the electron flux variations occur in the vertical axis (or in the axis perpendicular to the atmospheric slab). When the magnetic field is also horizontal, the problem becomes simply local at the scale of the free mean path of the electrons.

This explains why the TRANSCAR model is still valid at middle and low latitudes in the dayside of the Earth, as the results shown in Sect. 4.1 will confirm. This configuration had already been used to forecast the ionospheric production in the ionosphere of Titan (Galand et al., 1999).

3 WINDII observations

3.1 The instrument

The dayglow measurements are derived from the WIND Imaging Interferometer (WINDII), flying on board the NASA UARS satellite launched on 12 September 1991 and dedicated to middle atmosphere studies (Reber et al., 1993). The WINDII instrument is based on the concept of a field-widened Michelson interferometer first described by Bouchareine and Connes (1963), and implemented in a configuration later conceived by Hilliard and Shepherd (1966). The most detailed description of the instrument can be found in Shepherd et al. (1993). WINDII, which was jointly sponsored by the Canadian Space Agency and the French Centre National d'Etudes Spatiales, in collaboration with NASA, allows one to obtain the volume emission rates of the O(^{1}S), O(^{1}D), OH and O_2 lines, corresponding to an altitude ranging from 80 to 300 km. Error bars on the volume emission rates are about 1 to 10 photons.cm^{-3}.s^{-1}. All the data presented here are produced by the WINDII software version 5.11 and extracted from L2FD files that contain for a given day the field of view observations, i.e. altitude profiles of emission rates, temperatures and line of sight velocity along each orbit.

3.2 Altitude and emission at the maximum of the thermospheric layers

In order to calculate the intensity and altitude at the maximum of the O(^{1}D) and O(^{1}S) thermospheric layer, a least-squares fitting is performed on the emission rate altitude profiles, with respect to the shape of the considered emission.

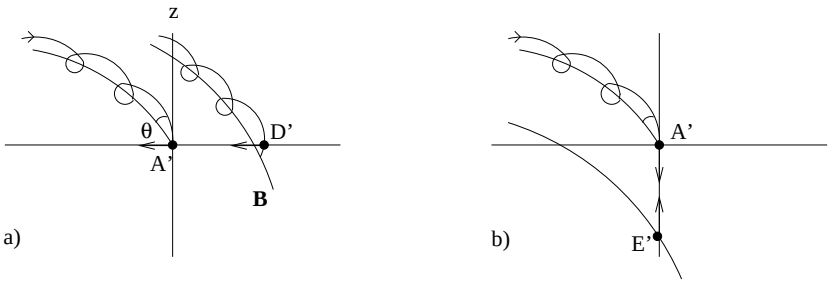

Fig. 4. Problem Geometry. The magnetic field has an magnetic dip angle θ at the observation point A$'$. The axis z represents the vertical axis and the abscissa is the horizontal.

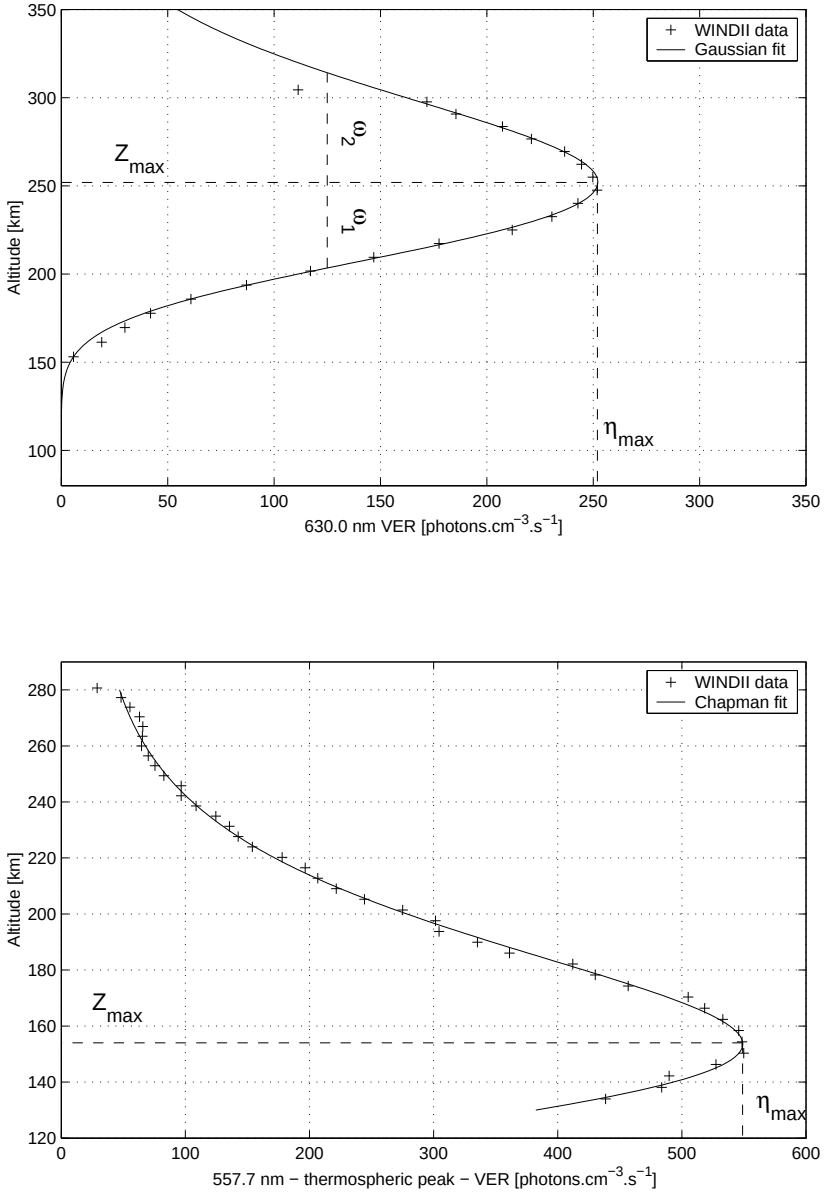

Fig. 5. The (top) 630.0 nm Volume Emission Rate fitted by a Gaussian function and (bottom) 557.7 nm thermospheric peak fitted by a chapman function.

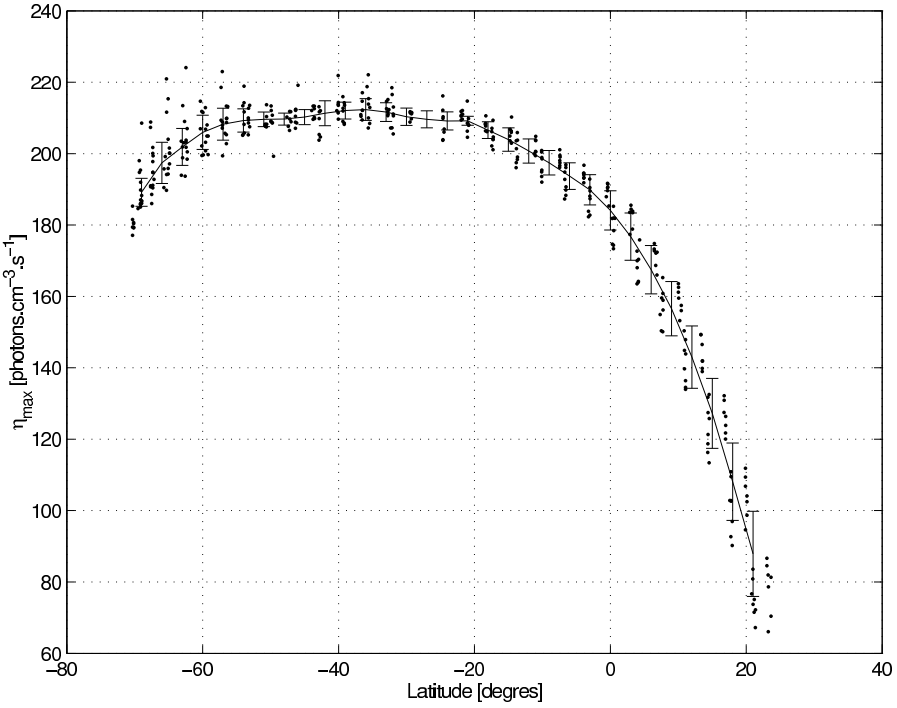

Fig. 6. WINDII data of the oxygen red emission measured on 1 April 1992 (A_p=13, $f_{10.7}$=191.4). Dots represent the WINDII 630.0 nm VER data plotted versus latitude, and the line represents the corresponding zonal average. Error bars indicate the standard deviation.

For the 630.0 nm red line emission, an asymmetrical Gaussian profile was used to describe the measurements (Thuillier et al., 1992). This function is represented by:

$$\eta(z) = \eta_{\max} exp\left(-\frac{1}{2}\left(\frac{z - z_{\max}}{x_1 + x_2 z}\right)^2\right), \quad (1)$$

where η is the volume emission rate, z is the altitude of the emission, x_1 and x_2 are calculated from w_1 and w_2 which represent the lower and upper width of the profile (see Fig. 5).

For the 557.7 nm green line thermospheric peak, the profiles are best fitted with a Chapman-like function written as follows:

$$\eta(z) = \eta_{\max} exp\,(1 - b - exp(-b))\,, \quad (2)$$

where $b = \frac{z - z_{\max}}{H}$, with H as the scale height of the Chapman profile.

This Chapman function was first exposed in Chapman (1931), and its ability to describe the oxygen green line thermospheric peak was discussed in Maharaj-Sharma and Shepherd (2002).

The examples in Fig. 5 show the good agreement between the theoretical profiles and the oxygen red and green lines layers. The top panel corresponds to the red line emission and the bottom one to the green line, with plus markers representing the WINDII data and the plain line representing the corresponding fit. For the entire set of data, we found a maximum deviation of less than 10% in the worst cases, between the WINDII measurements and the corresponding fit.

3.3 Zonal average

The WINDII data sampling pattern is determined by the interferometer viewing geometry and the UARS orbit characteristics. As described in Shepherd et al. (1993), WINDII observations are performed at the Earth limb in two directions, 45 and 135° with respect to the UARS velocity vector. The satellite orbit is circular (radius ∼585 km) and inclined at ∼57°. Its period is 96 min and its precession is about 20 min per day. This means that under ideal circumstances, a given latitude would be uniformly sampled (in Universal time and longitude) at about the same local time, about 15 times a day, for each of the upleg and downleg orbit segments, the data from each leg being about 12 h local time apart. In order to study the statistical variability of the dayglow with solar flux (solar activity and solar zenith angle), one has used a zonal average. This process averaged out any longitudinal variability associated with the dynamical processes, like tides and planetary waves, whose influence has been clearly identified on the O(^{1}S) night-time emission rate (Shepherd et al., 1997) and on the O(^{1}D) nightglow in the intertropical zone (Thuillier et al., 2002). Longitudinal variations of the O(^{1}S) dayglow are also presented in Shepherd et al. (1997) and Maharaj-Sharma (2003), and discussed in terms of planetary waves influence. This zonal average consists first in the interpolation of the measurements to regularly spaced latitudes, and then in taking a mean value at those given latitudes. This average requires a two-step process: one with all the peak data (height and intensity) for a given latitude, and thereafter a second step only taking into

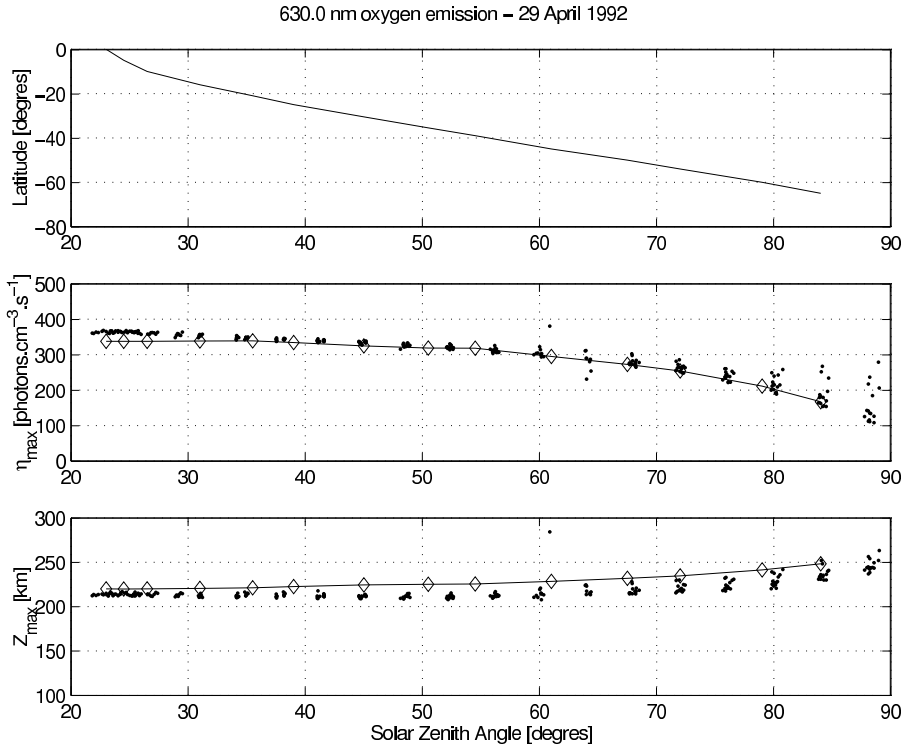

Fig. 7. 630.0 nm oxygen line – 29 April 1992 – $f_{10.7}$=128.5, A_p=7. Dots correspond to WINDII measurements and line/diamonds correspond to TRANSCAR results.

account the measurements within 2σ, σ being the standard deviation. This second mean allows us to remove a few bad data points. One example of a zonal mean can be seen in Fig. 6, which represents the 630.0 nm volume emission rate maximum, measured by WINDII on 1 April 1992. Individual measurements used in the mean being at most 20 min LT apart, correspond to Solar Zenith Angle values less than 3° apart at the equator and 5° apart at a latitude of 60° north or south.

4 Results

4.1 Modelling of the volume emission rate along the WINDII orbit

In this section we have chosen to present simulations of WINDII observations on two days for each thermospheric layer, one corresponding to low solar activity and the other to high solar activity. The results are presented as a function of SZA, which is one of the main parameters that controls the dayglow, together with solar activity. However, one has to keep in mind that each SZA corresponds to a given latitude, depending on the satellite orientation, and that the latitude is another parameter that influences the emission rates through the latitudinal variation of the neutral atmosphere. This is why on the following figures, the latitudinal extent of the measurements is also indicated. The WINDII data have not been zonally averaged to show the extent of the variability of the measurements along the different orbits.

4.1.1 The red line

Figures 7 and 8 show red line measurements taken on 29 April 1992, and 9 January 1995. The $f_{10.7}$ index for the first day was equal to 128.5, and the A_p index was 7, and for the second day we had $f_{10.7}$=73.7 and A_p=7. The upper panel shows the evolution of the latitude with regards to the SZA, the mid panel shows the maximum volume emission rate in photons.cm^{-3}.s^{-1} and the bottom panel corresponds to the altitude in kilometers of the red line emission maximum, both extracted using Eq. (1). For the VER and altitude panels, the dots represent the WINDII data and the diamond-shape curve corresponds to the TRANSCAR results. Those diamonds indicate the SZA for which the code was run, and the line is a linear interpolation of the model results between two runs.

The first noticeable characteristic is a reasonable agreement between the model results and WINDII data: TRANSCAR reproduces correctly the variation of the measurements with solar zenith angle, and this, for weak solar activity (on 9 January 1995), or for strong solar activity (on 29 April 1992).

When taking a closer look at the small solar zenith angles, one can notice a small discrepancy, with modeled VER being weaker than the ones measured by WINDII, by about 10%.

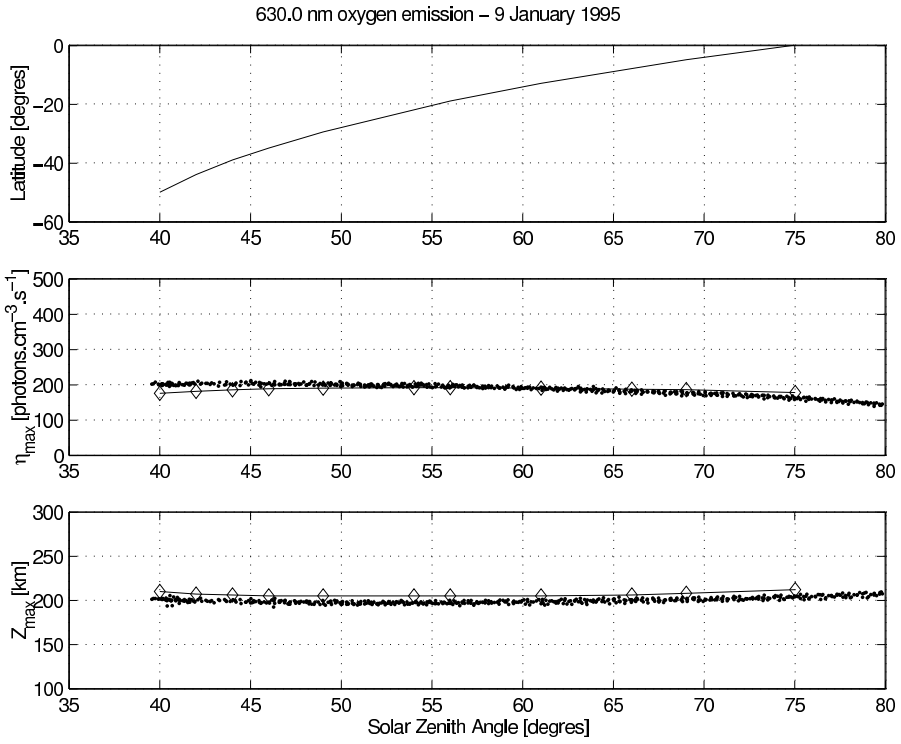

Fig. 8. 630.0 nm oxygen line – 9 January 1995 – $f_{10.7}$=73.7, A_p=7. Dots correspond to WINDII measurements and line/diamonds correspond to TRANSCAR results.

This underestimation corresponds to low latitudes on 29 April and on 9 January, the underestimation occurs on the contrary, at middle latitudes, which makes it impossible to explain the observed discrepancy with a variation in latitudes. Another point is that TRANSCAR does not yet take into account the influence of the photoelectrons produced in the conjugate hemisphere and transported along the magnetic field lines. But Torr et al. (1990) showed, taking the example of the $O^+(^2P)$ 732 nm and the $N_2(2P)$ 337.1 nm emissions which are mainly produced by the action of those energetic electrons, that the conjugate photoelectrons influence can only be seen during the night in the winter hemisphere. Thus, including a proper treatment of conjugate photoelectrons in TRANSCAR would not have been significant in the calculation of dayglow emissions. On the other hand, a possible cause of the discrepancy observed on the red line would be the weak representativity of the $f_{10.7}$ index with respect to the solar EUV activity, compared to the $MgII$ index, as discussed in Sect. 4.2. As the solar EUV influence is the most important for small solar zenith angles, this would explain why the discrepancy is mainly noticeable below SZA=45°.
TRANSCAR also over-evaluates slightly the peak altitude, with modelled altitudes higher than the measured ones of about 10 km. We note that 10 km is the order of magnitude of the variable altitude step of the model in the F-region, but we cannot assert that the 10 km discrepancy is due to the model height resolution. In Fig. 7 and Fig. 8, one can also notice the very low scattering of the measurements. Only for high latitudes on 9 April, this scattering increases. This low scattering which corresponds to very low longitudinal variations, justifies the zonal means used in the following statistics.

4.1.2 The green line

As for the red line, two dates are presented in order to study the variations of the 557.7 nm oxygen green emission: 25 October 1992 and 23 December 1995. Figures 9 and 10 show TRANSCAR results and WINDII data for those two days, and we remind the reader here that only the maximum of the thermospheric layer is presented on those plots. The $f_{10.7}$ index for the first day was equal to 146.8, and the A_p index was 7, and for the second day we had $f_{10.7}$=71.2 and A_p=8. Those two days were chosen for the similarities in the satellite orbits, with low solar zenith angles corresponding to low latitudes, and solar zenith angles greater than 60° corresponding to latitudes below 30° south, as shown on the upper panels of Figs. 9 and 10. The magnetic activity is also nearly identical, meaning that the main difference between those two sets of measurements comes from the solar flux intensity. For the strong solar flux conditions (25 October 1992), the measured volume emission rates are almost twice as strong as for the low solar conditions day (23 December 1995). Those large differences were properly reproduced by the TRANSCAR model. However, a small overestimation is noticeable at low latitudes, but it represents a deviation of less than 10% from the mean and remains inside the maximum WINDII values. Despite this discrepancy, TRAN-

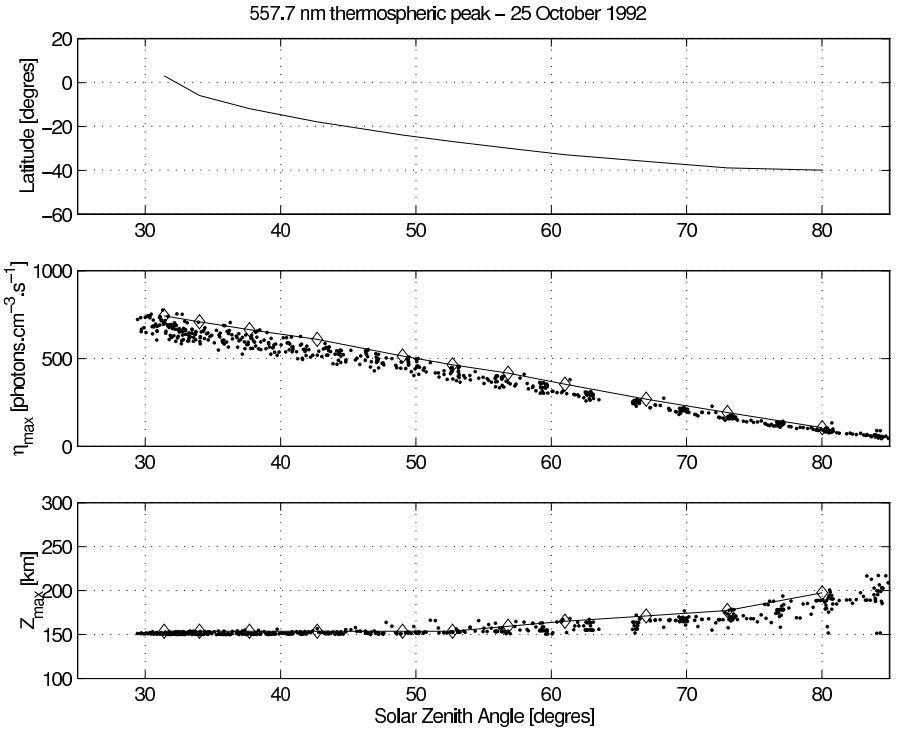

Fig. 9. 557.7 nm oxygen thermospheric line – 25 October 1992 – $f_{10.7}$=146.8, A_p=7. Dots correspond to WINDII measurements and line/diamonds correspond to TRANSCAR results.

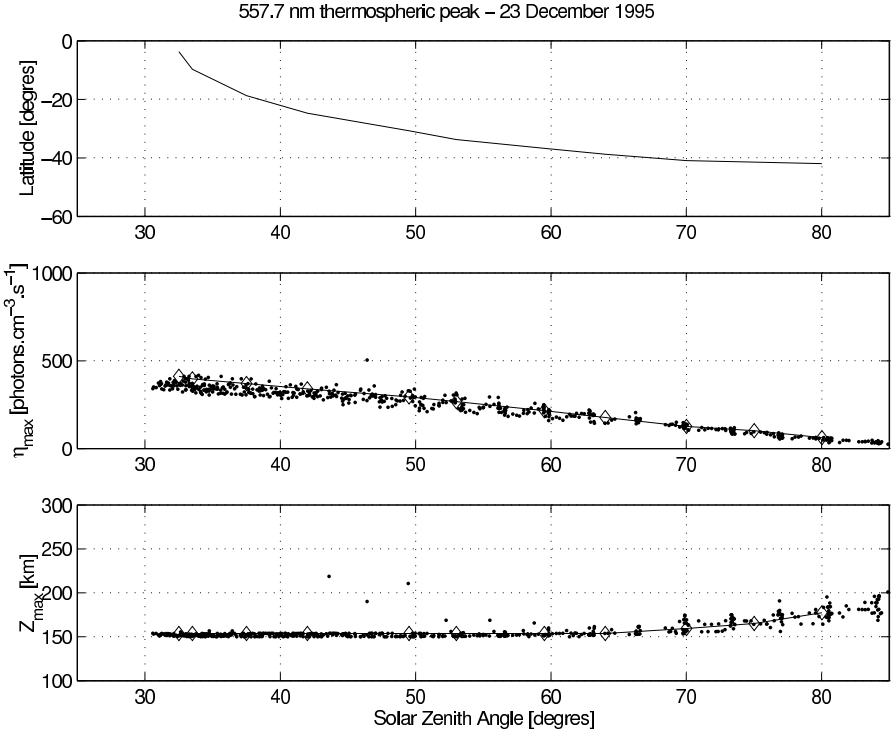

Fig. 10. 557.7 nm oxygen thermospheric line – 23 December 1995 – $f_{10.7}$=71.2, A_p=8. Dots correspond to WINDII measurements and line/diamonds correspond to TRANSCAR results.

Table 2. Geophysical parameters for the three selected days represented in the frame in Fig. 12. The first date corresponds to the point at the top of the frame and the last date to the point at the bottom.

day	630.0 nm VER peak ($cm^{-3}.s^{-1}$)	$MgII$	$f_{10.7}$	A_p	Latitude (degrees)
28 Dec. 1994	201.3	0.2585	75.9	10	46
21 Dec. 1994	199.8	0.2586	82.4	6	42
9 Jan. 1995	176.7	0.2585	73.7	7	−5

SCAR results reproduce reasonably well the maximum altitude and VER observed by WINDII, particularly on 23 December, where observations are less scattered. The larger scattering of WINDII data observed in O(^{1}S), as compared to O(^{1}D), is a general feature of the measurements and may be related to the greater importance of dynamical phenomena, such as tides and planetary waves in the lower thermosphere.

4.2 Statistical results

The atomic oxygen emissions data obtained with the WINDII interferometer from 1992 to 1995 are shown hereafter, and we stress that only quiet magnetic days are analysed ($A_p \leq 10$). This represents 22 days for the oxygen red emission line, and 97 for the green line. This small amount of red emission line data is due to the typical WINDII weekly schedule, with one day for the red line observations and three days for the green line observations, but with several periods without 630.0 nm measurements. We have chosen to present the zonal means of the maximum volume emission rates and maximum altitudes as a function of solar activity for three different solar zenith angles: 30, 50 and 70°. As was done in the simulations we used the $f_{10.7}$ index to represent the solar activity. We also chose to use the $MgII$ index (Cebula and DeLand, 1998) which is an alternative proxy for EUV solar flux. Thuillier and Bruinsma (2001) pointed out the superiority of the $MgII$ index over the $f_{10.7}$ index with respect to upper atmosphere heating processes, suggesting to use this former proxy for thermospheric modelling. Maharaj-Sharma and Shepherd (2003) in their study of the mesospheric and thermospheric O(^{1}S) dayglow examined 5 different proxies of the solar EUV flux, and found also slightly higher correlations with $MgII$ than with $f_{10.7}$ for the thermospheric layer.

4.2.1 The red line

Figure 11 shows the volume emission rates $\eta_{\max}$ and the emission maximum altitude $Z_{\max}$, extracted from the WINDII data using the method described in Sect. 3.2, as a function of $f_{10.7}$. Each one of the three plots stands for a different solar zenith angle, respectively, 30, 50 and 70° from top to bottom. Correlation coefficients of VER to $f_{10.7}$ (assuming a linear relationship) are indicated on the plots.

Looking at Fig. 11 and considering the intensity of the emission maximum, i.e. $\eta_{\max}$, one can see that it decreases with the increase of solar zenith angle. On the top panel (for a solar zenith angle of χ=30°), we have a mean value of roughly 300 photons.cm^{-3}.s^{-1}, while we have on the middle panel (χ=50°) roughly 250 photons.cm^{-3}.s^{-1}, and roughly 230 at χ=70° (bottom panel). This means a decrease of about 25% when going from a Sun almost at zenith to a grazing Sun. This result is not surprising because the larger the solar zenith angle, the larger the atmosphere layer and thus, the EUV flux decreases and the reaction involving electron impacts weakens. As previously seen in Fig. 2 this reaction is one of the preponderant production process involved in the red line emission. The solar zenith angle influence is very weak on the emission altitude, and the red line peak remains around 210 km high when solar zenith angle is smaller or equal to 70°.

Regarding the influence of the $f_{10.7}$ index, one can say that when the solar activity and then the EUV flux increases, a greater importance is given to the reaction involving electron impacts, and then the thermospheric peak is enhanced, as expected. When considering a solar zenith angle of 30°, the variation is quite strong: it increases from 230 to about 350 photons.cm^{-3}.s^{-1}, which is about 50% more, and we have variations of the same order for solar zenith angles of 50 and 70°. This rise with solar flux can also be seen with the altitude $Z_{\max}$ of the emission maximum, even if it is less pronouced than for the peak intensity, with a variation of about 10% with the increase of the $f_{10.7}$ index, no matter which solar zenith angle is considered. The results of the TRANSCAR simulation presented in Sect. 4.1.1 have been added in Fig. 11, as green diamonds. Additionnal TRANSCAR simulations for intermediate solar activity conditions are shown as red circles. Within the more global picture displayed by the statistics, one can say that TRANCAR is able to give a good picture of the main variations of the O(^{1}D) layer maximum, despite an offset present in the maximum emission altitude, as already noticed in Sect. 4.1.

Figure 12 shows the same WINDII volume emission rate and altitude data plotted this time versus the $MgII$ index. Correlations coefficients are significantly higher for the two smallest solar zenith angles, i.e. when the solar EUV influence is the most important. The remaining scattering of the points can be attributed to latitudinal and seasonal variations. We have examined all points with nearly the same $MgII$ index but different volume emission rates and have verified that in all cases the latitude and/or the season were different. A good example is given by the three points encircled in Fig. 12 (bottom panel). In Table 2 the A_p, $f_{10.7}$ and $MgII$ indices for those days are indicated, together with the latitude corresponding to the solar zenith angle of 70°. One can see that when the latitude and season are the same (two first points), the maximum VER are almost identical, however, this is not the case for the last point. Using the $f_{10.7}$ index would not have allowed such an analysis.

4.2.2 The green line

In Fig. 13 the results are presented for the atomic oxygen green thermospheric peak, in the same format as the red line. The green line behavior regarding the solar zenith an-

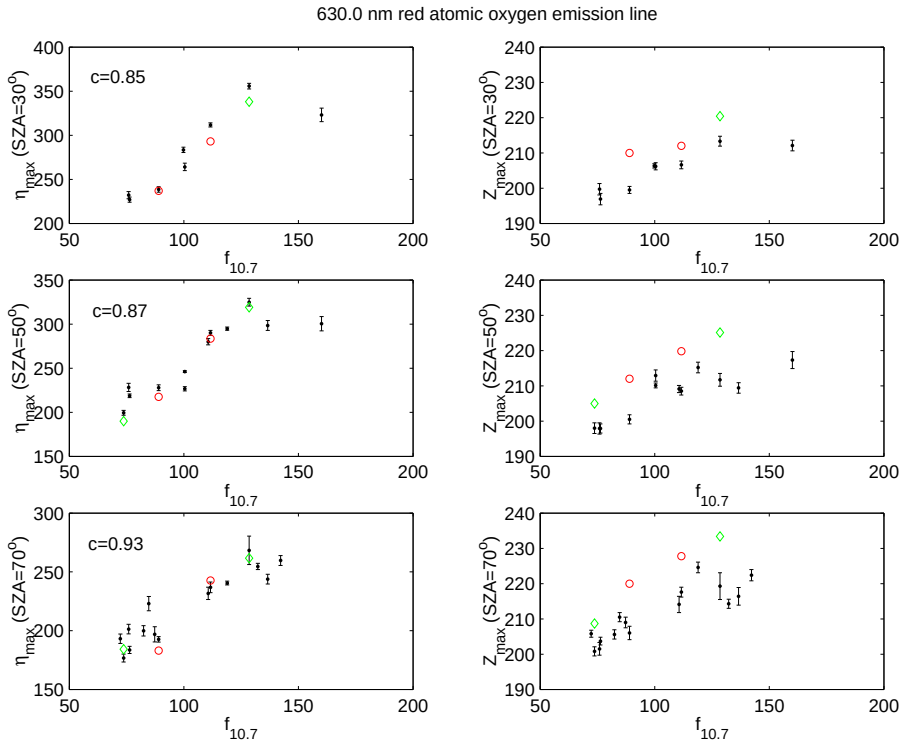

Fig. 11. WINDII measurements of the 630.0 nm volume emission rates and maximum emission altitudes for quiet geomagnetic days ($A_p \leq 10$), from 1992 to 1995. Data are plotted versus the $f_{10.7}$ index, and error bars correspond to the standard deviation. Diamonds correspond to the TRANSCAR simulation results presented in Sect. 4.1.1, and circles are simulations results for intermediate solar activity.

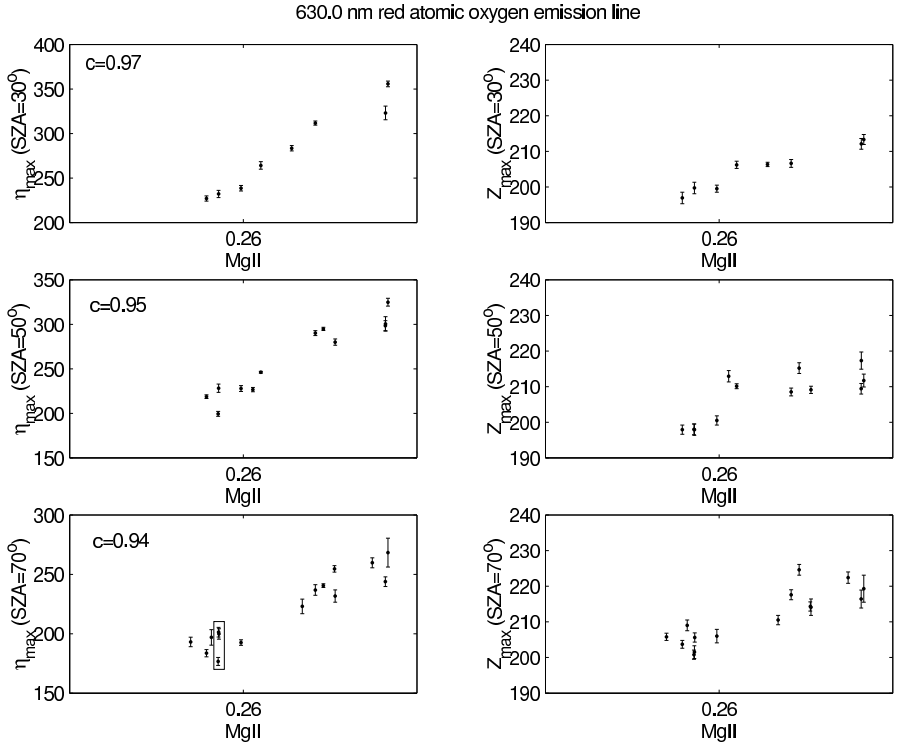

Fig. 12. WINDII measurements of the 630.0 nm volume emission rates and maximum emission altitudes for quiet geomagnetic days ($A_p \leq 10$), from 1992 to 1995. Data are plotted versus the $MgII$ index, and error bars correspond to the standard deviation.

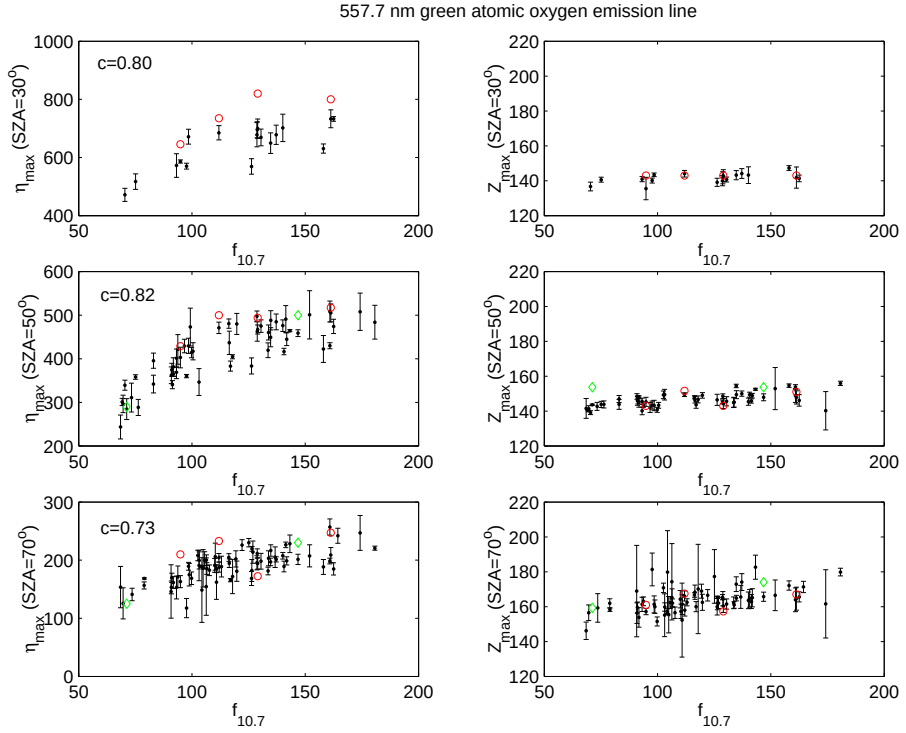

Fig. 13. WINDII measurements of the 557.7 nm (thermospheric peak) volume emission rates and maximum emission altitudes for quiet geomagnetic days ($A_p \leq 10$), from 1992 to 1995. Data are plotted versus the $f_{10.7}$ index, and error bars correspond to the standard deviation. Diamonds correspond to the TRANSCAR simulation results presented in Sect. 4.1.2, and circles are simulations results for intermediate solar activity.

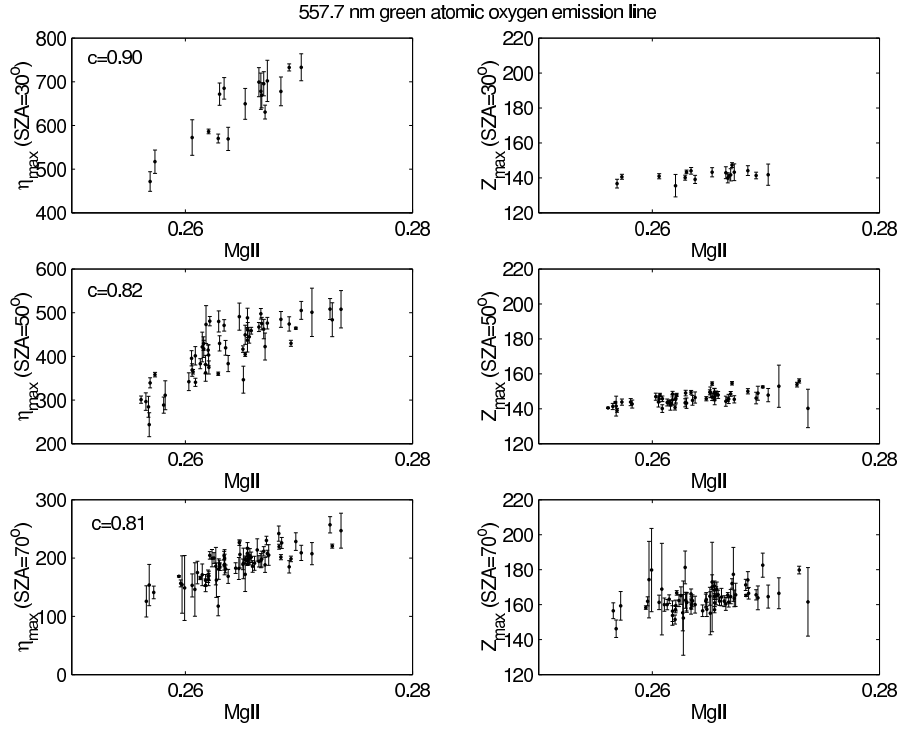

Fig. 14. WINDII measurements of the 557.7 nm (thermospheric peak) volume emission rates and maximum emission altitudes for quiet geomagnetic days ($A_p \leq 10$), from 1992 to 1995. Data are plotted versus the $MgII$ index, and error bars correspond to the standard deviation.

gle is quite similar to the 630.0 nm emission comportment, with a decrease in the emission intensity and an increase in the emission altitude with solar zenith angle. The decrease in emission intensity is strong, starting with a mean value of roughly 600 photons.cm^{-3}.s^{-1} at a solar zenith angle of χ=30° (upper panel), and ending with a mean value of roughly 200 photons.cm^{-3}.s^{-1} at a solar zenith angle of χ=70° (lower panel). For the emission altitude, a weak increase with solar zenith angle is noticeable, with an average peak altitude going up by 20 km when the solar zenith angle goes from 30 to 70°.

For the variations with solar activity, we have quite a strong fluctuation on the peak intensity: it goes from 500 photons.cm^{-3}.s^{-1} to 750 at solar zenith angle χ=30°, and we have variations of the same order for solar zenith angles of 50 and 70°. For the emission altitude, the variation with the solar flux is quite similar to the red line, with an increase of about 10%. Simulations results have been added as diamonds and circles in Fig. 13, as was done for the red line. As previously mentioned in Sect. 4.1.2, one immediately notices an overestimation of the intensities at SZA=30°. This overestimation is about 10% for three cases over four. For larger solar zenith angles, simulations and observations agree within about 10%. Concerning the maximum emission altitude, TRANSCAR gives a good representation of the measurements.

Figure 14 show the same data as a function of the $MgII$ proxy. The correlation coefficients are significantly higher for SZA, equal to 30° and 70°. At 50°, where the scattering of data is the largest, no real improvement is, however, observed.

5 Summary and conclusions

In order to summarize the behavior of the atomic oxygen emissions with regards to the solar zenith angle and the solar flux variations, one gives hereafter estimations of those parameters' influence and their physical interpretation:

1. when solar zenith angle increases from 30° to 70°,
   - the peak intensity decreases by about 25% for the red line, and 70% for the green line. This is mainly caused by the decrease of the EUV flux and then the frequency of the photoelectron impacts, one of the preponderant production processes for both emissions,
   - the peak altitude increases by 10% for the green line but remains nearly constant for the red line;
2. when solar activity increases by a factor of 3, red and green line emissions intensity and altitude increase (by about 50% and 10%, respectively, regardless to the line considered). This can be interpreted again as the enhancement of the reaction involving photoelectron impacts with the increase of the solar EUV flux,
3. a better representativity of the $MgII$ index was found when describing the relations between the oxygen emissions and the solar EUV activity, demonstrated by better correlations than with the $f_{10.7}$ proxy.

Those comportments related to the solar zenith angle and solar flux variations are appropriately reproduced by our 1-D fluid/kinetic model TRANSCAR, even if small dissimilarities are noticeable. Those discrepancies were mainly discussed in terms of the ability of the $f_{10.7}$ index to represent the solar EUV thermosphere input. Future simulation works will try to introduce a different proxy, such as $MgII$, as input to the neutral atmosphere model. It is likely to be done by using the new DTM-2000 model (Bruinsma et al., 2003) which uses this proxy, instead of the MSIS model which involves $f_{10.7}$.

Possible continuations for statistical data analysis could be first to quantify the influence of other geophysical parameters such as the latitude or seasonal variations. This can be performed only for the thermospheric O(^{1}S) layer, with the O(^{1}D) database being too small. A second interesting study would be to look at the oxygen dayglow variations during active magnetic periods. Reaching a better understanding of how the airglow fluctuates during magnetic disturbances would lead to a better knowledge of the high atmosphere response to geomagnetic activity, which is important for space weather users.

Acknowledgements. The WINDII project is sponsored by the Canadian Space Agency and the Centre National d'Etudes Spatiales (CNES). The authors would like to acknowledge the members of the WINDII team. Thanks are due to P.-L. Blelly for helpful discussions and to the reviewer for his assistance in evaluating the paper.

Topical Editor U.-P. Hoppe thanks J. Makela for his help in evaluating this paper.

References

Bouchareine, P. and Connes, P.: Interferometer with compensated field for Fourier transform spectroscopy, J. Phy., 24, 2, 134–138, 1963.

Bruinsma, S., Thuillier, G., and Barlier, F.: The DTM-2000 empirical thermosphere model with new data assimilation and constraints at lower boundary: accuracy and properties, J. Atmos. S.-P., 65, 1053–1070, 2003.

Cebula, R. P. and DeLand, M. T.: Comparisons of the NOAA-11 SBUV/2, UARS SOLSTICE and UARS SUSIM MgII solar activity proxy indices, Solar Phys., 177, 117–132, 1998.

Chamberlain, J. W.: Physics of the aurora and airglow, International Geophysics series, New York Academic Press, 1961.

Chapman, S.: The absorption and dissociative or ionizing effect of monochromatic radiation in an atmosphere on a rotating earth, Part II: Grazing incidence, Proceedings of the Physical Society, 43, 483–501, 1931.

Galand, M., Lilensten, J., Toublanc, D., and Sylvestre, M.: The ionosphere of Titan: ideal diurnal and nocturnal cases, Icarus, 140, 92–105, 1999.

Hays, P. B., Carignan, G., Kennedy, B. C., Shepherd, G. G., and Walker, J. C. G.: The visible airglow experiment on Atmosphere Explorer, Radio Sci., 8, 369, 1973.

Hedin, A. E.: Extension of the MSIS thermosphere model into the middle and lower atmosphere, J. Geophys. Res., 96, 1159–1172, 1991.

Hill, S. M., Solomon, S. C., Cleary, D. D., and Broadfoot, A. L.: Temperature dependance of the reaction $N_2(A^3\sum_u^+)$+O in the terrestrial thermosphere, J. Geophys. Res., 105, 10 615–10 630, 2000.

Hilliard, R. L. and Shepherd, G. G.: Wide-angle Michelson interferometer for measuring Doppler line widths, J. Opt. Soc. Am., 56, 362–369, 1966.

Lathuillère, C., Gault, W. A., Lamballais, B., Rochon, Y. J., and Solheim, B. H.: Doppler temperatures from O(^{1}D) airglow in the daytime thermosphere as observed by the WIND Imaging Interferometer (WINDII) on the UARS satellite, Ann. Geophys., 20, 203–212, 2002.

Lilensten, J. and Blelly, P.-L.: The TEC and F2 parameters as tracers of the ionosphere and thermosphere, J. Atmos. S.-P., 64, 775–793, 2002.

Maharaj-Sharma, R.: Solar variability of the atomic oxygen greenline emissions in the middle and lower thermosphere, Ph. D. Thesis, York University, 2002.

Maharaj-Sharma, R. and Shepherd, G. G.: Long term solar variability of the daytime atomic oxygen (O^{1}S) emission rate in the middle and lower thermosphere, J. Geophys. Res., 109, A3, A03303, doi:10.1029/2003JA010183, 2003.

Narayanan, R., Desai, J. N., Modi, N. K., Raghavarao, R., and Sridharan, R.: Dayglow photometry: a new approach, Applied Optics, 28, 2138–2142, 1989.

Opal, C. B., Peterson, W. K., and Beaty, E. C.: Measurement of secondary-electron spectra produced by electron impact ionization of a number of simple gases, J. of Chem. Physics, 55, 4100–4106, 1971.

Reber C. A., Trevathan, C. E., McNeal, R. J., and Luther, M. R.: The Upper Atmospheric Research Satellite (UARS) mission, J. Geophys. Res., 98, 10 643–10 647, 1993.

Richards, P. G., Fennelly, J. A., and Torr, D. G.: EUVAC: A solar EUV flux model for aeronomic calculations, J. Geophys. Res., 99, 8981–8992, 1994.

Shepherd, G. G., Thuillier, G., Gault, W. A., Solheim, B. H., Hersom, C., Alunni, J. M., Brun, J.-F., Brune, S., Charlot, P., Cogger, L. L., Desauliniers, D.-L., Evans, W. F. J., Girod, F., Gattinger, R. L., Harviee, D., Hum, R. H., Kendall, D. J. W., Llewellyn, E. J., Lowe, R. P., Ohrt, J., Pasternak, F., Peillet, O., Powell, I., Rochon, Y., Ward, W. E., Wiens, R. H., and Wimperis, J.: WINDII, the Wind Imaging Interferometer on the Upper Atmosphere Research Satellite, J. Geophys. Res., 98, 10 725–10 750, 1993.

Shepherd, G. G., Roble, R. G., McLandress, C., and Ward, W. E.: WINDII observations of the 558 nm emission in the lower thermosphere: the influence of dynamics on composition, J. Atmos. Terr. Phys., 59, 655–667, 1997.

Singh, V., McDade, I. C., Shepherd, G. G., Solheim, B. H., and Ward, W. E.: The O(^{1}S) dayglow emission as observed by the WIND imaging interferometer on the UARS, Ann. Geophys., 14, 637–646, 1996.

Singh, V. and Tyagi, S.: Testing of solar EUV flux models using 5577 Å, 6300 Å and 7320 Å dayglow emissions, Adv. in Space Research, 30, 11, 2557–2562, 2002.

Solomon, S. C. and Abreu, V. J.: The 630 nm dayglow, J. Geophys. Res., 94, 6817–6824, 1989.

Sridharan, R., Modi, N. K., Pallam Raju, D., Narayanan, R., Pant, T., Taori, A., and Chakrabarty, D.: Multiwavelength daytime photometer – a new tool for the investigations of the atmospheric processes, Measurement Science and Technology, 9, 585–591, 1998.

Taori, A., Sridharan, R., Chakrabarty, D., Modi, N. K., and Narayanan, R.: Significant upper thermospheric contribution to the O(^{1}S) 557.7 nm dayglow emission: first ground based evidence, J. Atmos. S.-P., 65, 121–128, 2003.

Thuillier, G. and Bruinsma, S.: The MgII index for upper atmosphere modelling, Ann. Geophys., 19, 219–228, 2001.

Thuillier, G., Christophe, J., Azria, G., Herse, M., Fauliot, V., Girod, F., Fratter, C., Thouvenin, J.-P., and Solheim, B. H.: Simulation of the experiment data from WINDII flown on the UARS/NASA satellite, Simulation, 59, 78–91, 1992.

Thuillier, G., Wiens, R. H., Shepherd, G. G., and Roble, R. G.: Photochemistry and dynamics in thermospheric intertropical arcs measured by the WIND Imaging Interferometer on board UARS: a comparison with TIE-GCM simulations, J. Atmos. S.-P., 64, 405–415, 2002.

Torr, M. R., Torr, D. G., Richards, P. G., and Yung, S. P.: Mid- and low-latitude model of thermospheric emissions, 1. $O^+(^2P)$ 7320 Å and $N_2(2P)$ 3371 Å, J. Geophys. Res., 95, 21 147–21 168, 1990.

Tyagi, S. and Singh, V.: The morphology of oxygen greenline dayglow emission, Ann. Geophys., 16, 1599–1606, 1998.

Upadhayaya, A. K. and Singh, V.: Effects of temperature dependance of reaction $N_2(A^3\sum_u^+)$+O on greenline dayglow emission, Ann. Geophys., 20, 2039–2045, 2002.

Witasse, O., Lilensten, J., Lathuillère, C., and Blelly, P.-L.: Modelling the OI 630.0 and 557.7 nm thermospheric dayglow during EISCAT-WINDII coordinated measurements, J. Geophys. Res., 104, 24 639–24 656, 1999.